nature chemical biology

ARTICLES

https://doi.org/10.1038/s41589-018-0032-5

Super-long single-molecule tracking reveals dynamic-anchorage-induced integrin function

Taka A. Tsunoyama[1], Yusuke Watanabe[2], Junri Goto[2], Kazuma Naito[2], Rinshi S. Kasai[3], Kenichi G. N. Suzuki[2,4], Takahiro K. Fujiwara[2] and Akihiro Kusumi[1,2,3]*

Single-fluorescent-molecule imaging tracking (SMT) is becoming an important tool to study living cells. However, photobleaching and photoblinking (hereafter referred to as photobleaching/photoblinking) of the probe molecules strongly hamper SMT studies of living cells, making it difficult to observe in vivo molecular events and to evaluate their lifetimes (e.g., off rates). The methods used to suppress photobleaching/photoblinking in vitro are difficult to apply to living cells because of their toxicities. Here using 13 organic fluorophores we found that, by combining low concentrations of dissolved oxygen with a reducing-plus-oxidizing system, photobleaching/photoblinking could be strongly suppressed with only minor effects on cells, which enabled SMT for as long as 12,000 frames (~7 min at video rate, as compared to the general 10-s-order durations) with ~22-nm single-molecule localization precisions. SMT of integrins revealed that they underwent temporary (<80-s) immobilizations within the focal adhesion region, which were responsible for the mechanical linkage of the actin cytoskeleton to the extracellular matrix.

Fluorescence microscopy is extensively used in biomedical research with living cells. In particular, SMT of fluorescent molecules at work in living cells is now providing researchers with the unprecedented ability to directly observe molecular dynamics and interactions. However, SMT and fluorescence microscopy are greatly hampered by photobleaching/photoblinking of the fluorescent probe molecules[1–6]. For example, the durations of molecular events, such as transient immobilizations, could in principle be directly measured by SMT; however, photobleaching/photoblinking make such measurements quite difficult.

Numerous methods have been devised to reduce photobleaching/photoblinking, including deoxygenation[7,8], the addition of reducing reagents and the addition of both reducing and oxidizing reagents, which is referred to as the reducing-plus-oxidizing system (ROXS)[9,10] (Supplementary Fig. 1); however, these methods are generally quite difficult to apply to living cells because of their toxicity. Therefore, here our aim was to develop (i) a method to suppress photobleaching/photoblinking of fluorescent organic molecules and (ii) a theory to determine the lifetimes of molecular events by SMT in the presence of photobleaching/photoblinking during the limited observation period (Supplementary Fig. 2). The method developed, super-long imaging-tracking of single individual molecules, was applied to investigate how β_1 and β_3 integrins, which are transmembrane receptors for the extracellular matrix (ECM) in focal adhesions (FAs), mechanically link the ECM and actin filaments in the cytoplasm, at the level of single molecules.

Results

ROXS and lower oxygen concentrations used in this research. The photobleaching rates of nine fluorescent organic compounds, as well as four organic fluorophores that were conjugated to the synthetic antioxidant trolox, were examined at the single-molecule level at 37 °C in living cells. Each of these was covalently linked to a tag protein (acyl carrier protein (ACP) or Halo) that was fused to the five-path transmembrane protein CD47 at its N-terminal extracellular domain or its C-terminal cytoplasmic domain (only for the Halo-tagged protein) and was expressed in the plasma membrane (PM) of T24 human epithelial cells.

Molecular oxygen is completely removed in many photobleaching- and photoblinking-suppression methods. However, here we optimized the concentration of molecular oxygen, as molecular oxygen is essential for cell survival and might be useful for shortening the triplet-state lifetime (see Supplementary Fig. 3 and the Methods for the method used to control or measure the concentrations of dissolved oxygen in the medium). In the following part of this report, we describe the molecular oxygen concentrations in the cell culture medium as the percentages (partial pressure) of the molecular oxygen in the equilibrating gas mixture when its pressure was 760 mm Hg, and we express them in the manner '2%O_2' (no space between % and O_2) to indicate that the partial oxygen pressure was normalized to that under the 760 mm Hg atmosphere.

At the same time, we used ROXS. ROXS induces the transitions of fluorescent molecules in the triplet state to the ground state by way of the ion states by consecutive reduction (oxidation) and oxidation (reduction) reactions, thus effectively suppressing photobleaching/photoblinking (Supplementary Fig. 1). We used the less toxic compounds trolox, a vitamin E derivative, as a reducer and troloxquinone, a trolox derivative, as an oxidizer[11] at a fixed total concentration of 1 mM. The ROXS conditions used throughout are described as TX (1 mM trolox), TQ20 (0.8 mM trolox + 0.2 mM troloxquinone) and TQ40 (0.6 mM trolox + 0.4 mM troloxquinone) (Supplementary Fig. 4). The 'control' experiments were always performed in the absence of ROXS under 21%O_2.

ROXS + lower oxygen concentrations improves photostability. First, we describe the results obtained with tetramethylrhodamine (TMR) and SeTau647 (ST647), as these resulted in the largest improvements among the membrane-permeable and membrane-impermeable dyes, respectively. TMR and ST647 were conjugated to

[1]Membrane Cooperativity Unit, Okinawa Institute of Science and Technology Graduate University (OIST), Onna, Japan. [2]Institute for Integrated Cell-Material Sciences (WPI-iCeMS), Kyoto University, Kyoto, Japan. [3]Institute for Frontier Life and Medical Sciences, Kyoto University, Kyoto, Japan. [4]Present address: Center for Highly Advanced Integration of Nano and Life Sciences (G-CHAIN), Gifu University, Gifu, Japan. *e-mail: akihiro.kusumi@oist.jp

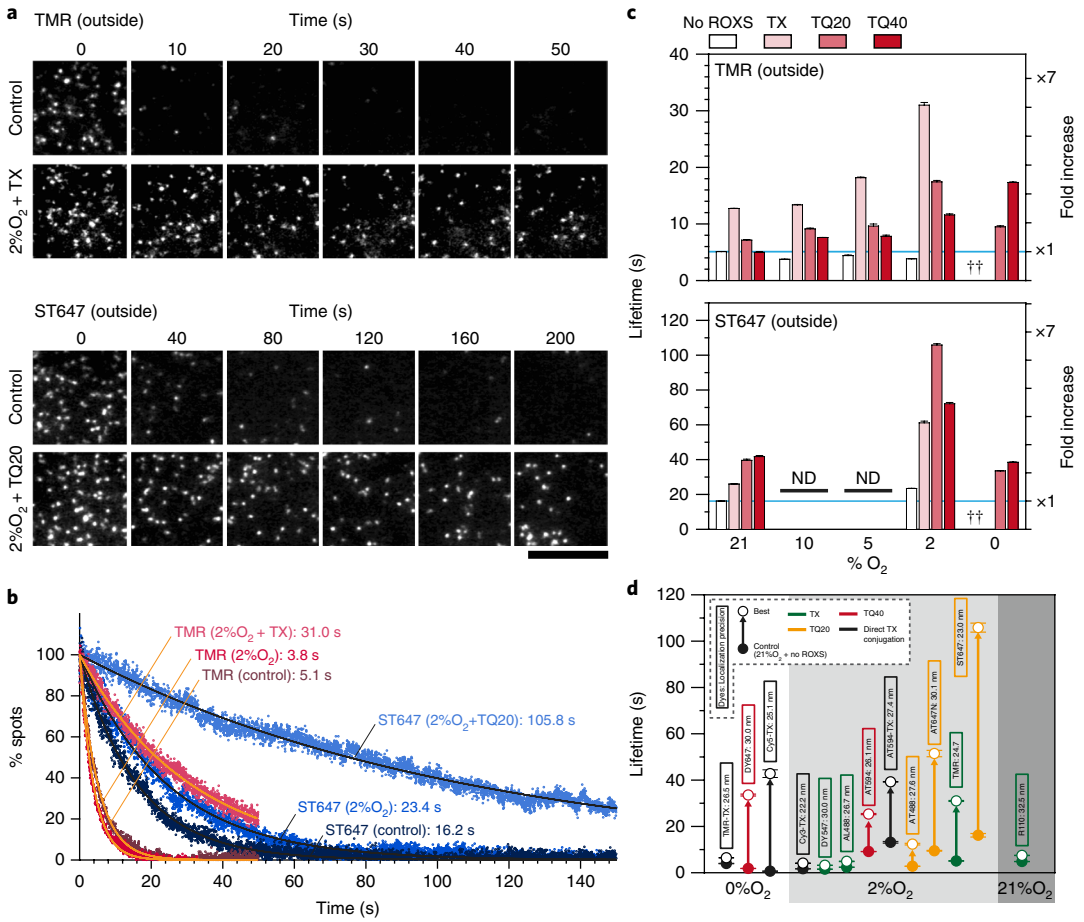

Fig. 1 | Photobleaching lifetimes in single-fluorescent-molecule imaging are prolonged under the conditions of low O_2+ROXS. a, Representative total internal reflection fluorescence (TIRF) microscopic images (among six independent experiments) of a time series for TMR bound to Halo-CD47 (top) and ST647 bound to ACP-CD47 (bottom) (fluorophores located on the outer surface of a T24 epithelial cell). Note that the time scale for ST647 is lengthened by a factor of 4 from that for TMR. Scale bar, 10 µm. **b**, Time-dependent reductions of the numbers of fluorescence spots found in each 33-ms frame for TMR and ST647 on the extracellular surface (for the number of points, *n*, see Supplementary Table 1). Orange and black curves represent the best-fit single-exponential functions for TMR and ST647, respectively. The exponential decay time constants are shown in the figure. **c**, The photobleaching lifetime (exponential decay time constant) obtained by fitting with a single exponential function (Methods) under various $\%O_2$ and ROXS conditions for TMR (top) and ST647 (bottom) located outside the cell. Data are means ± s.e.m. (for the number of points, *n*, see Supplementary Table 1). A dagger symbol indicates that we were unable to determine these values owing to extensive blinking, which provided trajectories mostly as short as 1 or 2 frames (33 and 66 ms) that could not be distinguished from the noise signal. ND, not done. **d**, Summary of photobleaching lifetimes (exponential decay time constants) under control conditions and conditions for the slowest photobleaching (see Supplementary Table 1 for a comprehensive list, including the numbers of examined fluorescence spots and the degree of freedom for curve fitting; also see Supplementary Fig. 7). Most dyes exhibited the longest photobleaching time at $2\%O_2$, but some dyes did so at $0\%O_2$ and only the R110 dye exhibited the best performance under the control conditions ($21\%O_2$), with various ROXS conditions. All dyes were located on the outer surface of the cell. Data are means ± s.e.m.

Halo-CD47 and ACP-CD47, respectively (the comparison between Halo and ACP will be discussed later).

Typical time series analyses of single-molecule images of TMR and ST647 (Fig. 1a and Supplementary Videos 1 and 2) indicated that, when the ROXS and oxygen concentrations were adjusted, photobleaching could be greatly suppressed. The number of fluorescence spots found in each video frame plotted against time could be fitted by single-exponential functions (Fig. 1b and Supplementary Fig. 5). The exponential lifetimes evaluated under various O_2+ROXS conditions (at the same excitation laser power) are summarized in Fig. 1c (number counting photobleaching lifetime, which is almost the same as the lifetime evaluated by the bulk intensity measurements). In the case of TMR (or ST647), under the optimal conditions of $2\%O_2$+TX ($2\%O_2$+TQ20 for ST647), the photobleaching lifetime was prolonged up to 31.0 s (105.8 s for ST647), an increase in the lifetime by a factor of 6.1 (6.5 for ST647), at single-molecule localization precisions of 24.7 nm (control) and 25.8 nm ($2\%O_2$+TX) (23.0 nm (control) and 21.5 nm ($2\%O_2$+TQ20) for ST647) (Supplementary Fig. 6a–c (in which the signal intensities largely remained the same)). The photobleaching lifetime, fluorescence intensity and single-molecule localization precisions obtained under the control and optimized conditions are summarized in Table 1 (see also Supplementary Fig. 7 and Supplementary Table 1 (in which an extensive summary is provided)). Note that, for ease of the experiment, we kept the excitation laser intensity the same for the same dye molecule and that when we report the photobleaching lifetime we always specify the single-molecule localization precisions (21.5–32.5 nm, depending on the dye).

TMR attached to CD47-Halo, where the Halo-tagged protein is located in the cytoplasm, showed photobleaching lifetimes and signal intensities very similar to those of TMR bound to Halo-CD47 in the extracellular space (Supplementary Fig. 8). These results indicate

Table 1 | Photobleaching lifetimes using single-molecule imaging

Tag dye	Outside or inside the cell	Live or fixed cells	O_2 (%)	ROXS	Photobleaching lifetime (s) (by number counting)[a]	Relative prolongation (fold)[a]	Tracking lifetime (s)[b]	Relative intensity (fold)[c]	Localization precision (nm)
Halo-TMR	Outside	Live	21	–	5.1 ± 0.03	1.0 ± 0.01	–	1.0 ± 0.02	24.7
			21	TX	12.7 ± 0.04	2.5 ± 0.02	–	1.0 ± 0.01	–
			2	TX	31.0 ± 0.47	6.1 ± 0.10	–	0.9 ± 0.01	25.8
			0	TX	NA[d]		–	NA[d]	–
Halo-TMR	Outside	Fixed	21	–	4.6 ± 0.11	1.0 ± 0.03	4.3 ± 0.1	1.0 ± 0.01	24.7
			21	TX	12.2 ± 0.27	2.6 ± 0.05	10.7 ± 0.3	1.0 ± 0.01	–
			2	TX	29.1 ± 0.50	6.3 ± 0.19	23.7 ± 0.7	0.9 ± 0.01	25.8
			0	TX	NA[d]		0.9 ± 0.1	NA[d]	–
Halo-TMR	Inside	Live	21	–	5.3 ± 0.02	1.0 ± 0.01	–	1.0 ± 0.01	24.7
			21	TX	6.5 ± 0.09	1.4 ± 0.02		1.0 ± 0.01	–
			2	TX	32.4 ± 0.37	7.0 ± 0.08	–	0.9 ± 0.02	27.0
			0	TX	NA[d]		–	NA[d]	–
ACP-ST647	Outside	Live	21	–	16.2 ± 0.06	1.0 ± 0.01	–	1.0 ± 0.02	23.0
			21	TQ20	39.6 ± 0.69	2.4 ± 0.04	–	1.1 ± 0.03	–
			2	TQ20	105.8 ± 0.78	6.5 ± 0.05	–	1.4 ± 0.01	21.5
			0	TQ20	33.5 ± 0.12	2.1 ± 0.01	–	1.3 ± 0.01	–
ACP-ST647	Outside	Fixed	21	–	15.5 ± 0.11	1.0 ± 0.01	10.9 ± 0.2	1.0 ± 0.01	23.0
			21	TQ20	42.1 ± 0.66	2.7 ± 0.05	38.4 ± 1.3	1.1 ± 0.01	–
			2	TQ20	99.0 ± 1.57	6.4 ± 0.11	83.4 ± 2.1	1.4 ± 0.01	21.5
			0	TQ20	47.2 ± 1.30	3.0 ± 0.09	30.9 ± 0.8	1.3 ± 0.02	–

Photobleaching lifetimes obtained by counting the number of fluorescence spots in each image (number counting lifetime) and those obtained by tracking each individual molecule (tracking lifetime, which is affected by photoblinking) of TMR and ST647 under representative oxygen and ROXS conditions using single-molecule imaging are shown. For the number of points for estimation of the photobleaching lifetime by number counting, see Supplementary Table 1. [a]Exponential-decay time constant (means ± s.e.m.) (Methods). [b]Exponential-decay time constant (means ± s.e.m.). Single molecules blink, and therefore the duration from the initiation of the observation until the beginning of the first dark period for each molecule was measured. The determination of the single-molecule tracking lifetime was performed for only fixed cells for which CD47 was immobilized on the cell surface, to avoid possible complexity due to intermixing of blinking with other tracking problems. The numbers of molecules examined (in fixed cells, for the estimation of single-molecule tracking lifetimes) were as follows: 1,209, 988, 2,446, and 313 for TMR under control conditions, 21%O_2+TX, 2%O_2+TX, and 0%O_2+TX, and 750, 1,603, 1,884, and 1,741 for ST647 under control conditions, 21%O_2+TQ20, 2%O_2+TQ20, and 0%O_2+TQ20, respectively. [c]The modes ± s.e.m. obtained from the log-normal fitting (see the legend to Supplementary Fig. 6b). [d]NA, not analyzed owing to extensive blinking ('bright' periods generally lasting <66 ms; Methods).

that the reductive conditions in the cytoplasm (due to the presence of glutathione) did not affect photobleaching and ROXS efficacy. They also suggest that trolox and troloxquinone are membrane permeable.

The photobleaching lifetime of TMR-ACP-CD47 was shorter by a factor of ~3, as compared with that of TMR-Halo-CD47, and only a slight improvement was found after treatment with 2%O_2+TX. The reason for this difference is unknown. Meanwhile, when the membrane-impermeable dyes ATTO594 (AT594) and ST647 were conjugated to ACP-CD47 or Halo-CD47, the photobleaching lifetimes of the dyes bound to the ACP and Halo proteins were about the same (Supplementary Fig. 9 and Supplementary Table 1).

Single ST647 molecules can be imaged for ~3,200 frames. Among the 13 organic fluorescent compounds examined in this study (Fig. 1d), ST647 under optimal conditions (2%O_2+TQ20) exhibited the best photobleaching performance, with the exponential lifetime prolonged to 105.8 s from 16.2 s (6.5-fold difference; ~3,200 frames) at a single-molecule localization precision of 21.5 nm (Fig. 1d and Supplementary Fig. 6a). Note that, owing to rapid photoblinking, the photobleaching lifetimes of ST647 could not be properly determined with 0%O_2+TX or in the absence of ROXS. Rapid photoblinking was also observed with TMR under the same conditions (Methods). These conditions might be useful for direct stochastic optical reconstruction (dSTORM)-type observations.

Low O_2 + ROXS strongly suppresses photoblinking. Photoblinking is another serious problem in SMT. To avoid erroneous intermixing of blinking with other tracking problems, cells were fixed to immobilize CD47 on the cell surface. The fluorescence intensities of fixed single molecules as a function of time exhibited a single-step transition to a non-fluorescent state, due to either photobleaching or photoblinking (Supplementary Fig. 10). We measured the duration from observation initiation by turning on the excitation laser until the first transition to the dark state for each molecule, and after observing many single molecules we obtained the histogram for 'bright'-state durations (Fig. 2a). This histogram might be close to the on-time distributions, but it is more relevant to actual experiments conducted using live cells, as it provides the distribution of the lengths of single-molecule trajectories observed from time 0.

We found that the distributions could operationally be fitted by single-exponential functions ('single-molecule tracking lifetime'). Under the optimal conditions shown in Fig. 1b, the decay lifetimes were 23.7 s for TMR under 2%O_2+TX and 83.4 s for ST647 under 2%O_2+TQ20. These values are 10–20% shorter than the bulk photobleaching lifetimes (Fig. 2b,c and Table 1), probably owing to photoblinking. Nevertheless, under these conditions, single molecules of TMR and ST647 could be tracked longer than previously reported.

When TMR-Halo-CD47 was observed at higher camera frame rates of up to 10 kHz (Supplementary Fig. 11), with higher laser excitation conditions to provide similar single-molecule localization precisions, photoblinking was observed in the recordings at a 10-kHz frame rate. However, the dark periods lasted for 0.22 and 0.26 ms, in contrast to the 18 and 59 ms of the bright 'on' periods (exponential lifetimes; control and 2%O_2+TX conditions, respectively), suggesting

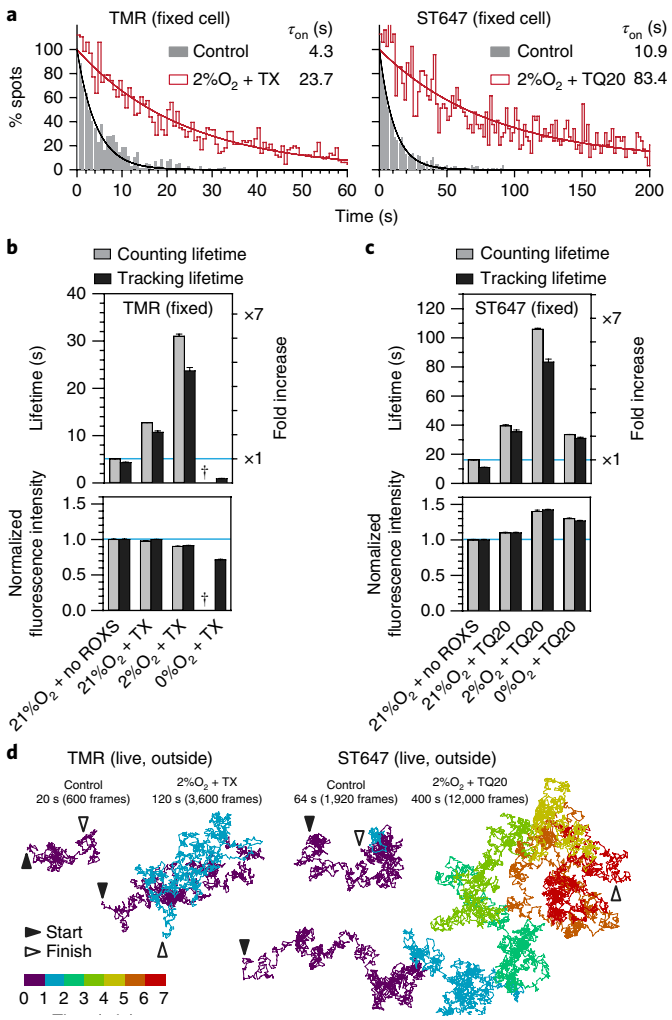

Fig. 2 | Photoblinking, in addition to photobleaching, can be suppressed under the optimal conditions of low oxygen concentrations+ROXS, as observed by single-fluorescent-molecule tracking at video rate. a, The distributions of bright-state durations of single TMR bound to Halo-CD47 (left) and ST647 bound to ACP-CD47 (right) molecules in fixed cells, observed at video rate, registered from time 0 of laser excitation and recording. Because single-molecule tracking ended at the moment the photoblinking (transition to the dark state) occurred, the lifetimes found by this method were shorter than those determined by counting the number of spots in each frame (Fig. 1a,b). The best-fit single-exponential curves are shown. The numbers of molecules examined are summarized in Table 1 (footnote b). **b,c**, Summary of photobleaching lifetimes obtained either by counting the number of fluorescence spots (counting lifetime) or from the duration distributions of single-molecule trajectories (tracking lifetime) (exponential-decay time constant) (means ± s.e.m.), as well as the fluorescence intensities (modes ± s.e.m. obtained by log-normal fitting; Supplementary Fig. 6b). A dagger symbol indicates that we were unable to measure these values owing to extensive blinking. For *n* values, see Table 1 (footnote b) and Supplementary Table 1. **d**, Typical trajectories for TMR and ST647 molecules linked to CD47 in the live cell PM that could be tracked without photoblinking and photobleaching for periods longer than 120 and 400 s (~4× lifetimes shown in Table 1, and thus representative among a few percent of molecules). Note the differences in the lengths of the trajectories obtained in the ambient atmosphere (control) versus those under the optimized conditions. Scale bar, 10 μm.

that such photoblinking will not strongly affect the observations at frame rates up to ~300 Hz (3.3-ms integration time > 10 × 0.26 ms).

In optimal cases, we found that single CD47 molecules could be tracked for 2 and 6.7 min at video rate using TMR and ST647, respectively, under their optimal conditions (Fig. 2d). Such long-term single-molecule observations would be extremely useful for studies of molecular interactions.

Strong cytotoxicity occurs at 0%O_2 but not at 2%O_2. First, under conditions with 2%O_2, T24, HeLa, CHO-K1 and NIH3T3 cells grew well. Their doubling times were comparable to those under the 5%O_2 and 21%O_2 conditions (Fig. 3a and Supplementary Fig. 12), consistent with previous observations[12].

Second, the effect of low oxygen concentrations on cell survival was examined in the microscope observation medium (Hank's balanced salt solution (HBSS) buffered with 2 mM *N*-Tris(hydroxymethyl)methyl-2-aminoethanesulfonic acid (TES, pH 7.4); hereafter referred to as T-HBSS) at 37 °C (Fig. 3b,c and Supplementary Fig. 13). At 2%O_2, almost all of the cells survived; however, at 0%O_2, the half-lives of the cells were only ~3.5 h.

Third, the influence of low oxygen concentrations on cellular activities was investigated by monitoring cell spreading. The time course of cell spreading was observed using β_1 integrin–deficient mouse embryonic fibroblasts (*Itgb1*-knockout MEFs; hereafter referred to as β_1-KO MEFs)[13] that had not or had been transfected with *Itgb1* (hereafter referred to as β_1-transfected MEFs; Fig. 3d and Supplementary Fig. 14a). The β_1-transfected MEFs spread faster than the β_1-KO MEFs, by a factor of ~2.5. The extent of cell spreading at 2%O_2 was almost the same as that at 21%O_2; however, at 0%O_2, it was diminished by 30–40% (statistically significantly), which was clear even at 15 min (observed for up to 90 min; Fig. 1d).

Fourth, the diffusion coefficients of CD47-mGFP in T24 and HeLa cells remained the same at 2%O_2; however, at 0%O_2 (even for 15 min), the diffusion coefficients in HeLa cells were greatly increased (although those in T24 cells were unaffected), consistent with the previous result[14] (Fig. 3e and Supplementary Figs. 15 and 16). According to our proposed picket-fence model[15], the increases in the diffusion coefficients found here are consistent with subtle depolymerization of the actin membrane skeleton.

Therefore, we conclude that for studies of living cells 0%O_2 should not be used and that 2%O_2 is quite suitable or even better than 21%O_2, consistent with previous observations[12,16]. Cells still thrive at lower oxygen concentrations, perhaps because of less peroxidation and/or the expression of hypoxia-inducible factor[17]. Indeed, the oxygen concentrations in animal tissues are generally much lower than 21%O_2[18–20].

Cytotoxicity of ROXS. Under the conditions of 2%O_2+ROXS, unlike that at 0%O_2, the reduction in the number of live T24 and HeLa cells became detectable only after 5, 6 and 7 h of incubation in the presence of TQ40, TQ20 and TX, respectively (Fig. 3b,c and Supplementary Fig. 13), and the diffusion coefficient of CD47-mGFP in the PM of these cells remained the same for 120 min (the longest incubation time used; Fig. 3e and Supplementary Figs. 15 and 16), indicating that ROXS did not change the physical properties of the PM during this period (however, see ref. [21]).

Similarly, under the conditions of 2%O_2+ROXS, unlike that at 0%O_2, the spreading of β_1-KO MEFs and β_1-transfected MEFs remained basically the same as under control conditions for 90 min (the longest incubation time used) (Fig. 3d and Supplementary Fig. 14a). Because our fluorescence observations were finished mostly within 15 min of the addition of ROXS (at 2%O_2), its toxic effect on our observations was predicted to be limited.

Comparison with dye molecules directly conjugated to trolox. Previously, other groups directly linked triplet-state quenchers (TSQs; such as cyclooctatetraene, 4-nitrobenzyl alcohol or trolox (TX)) to cyanine dyes and found that the photostabilities of the

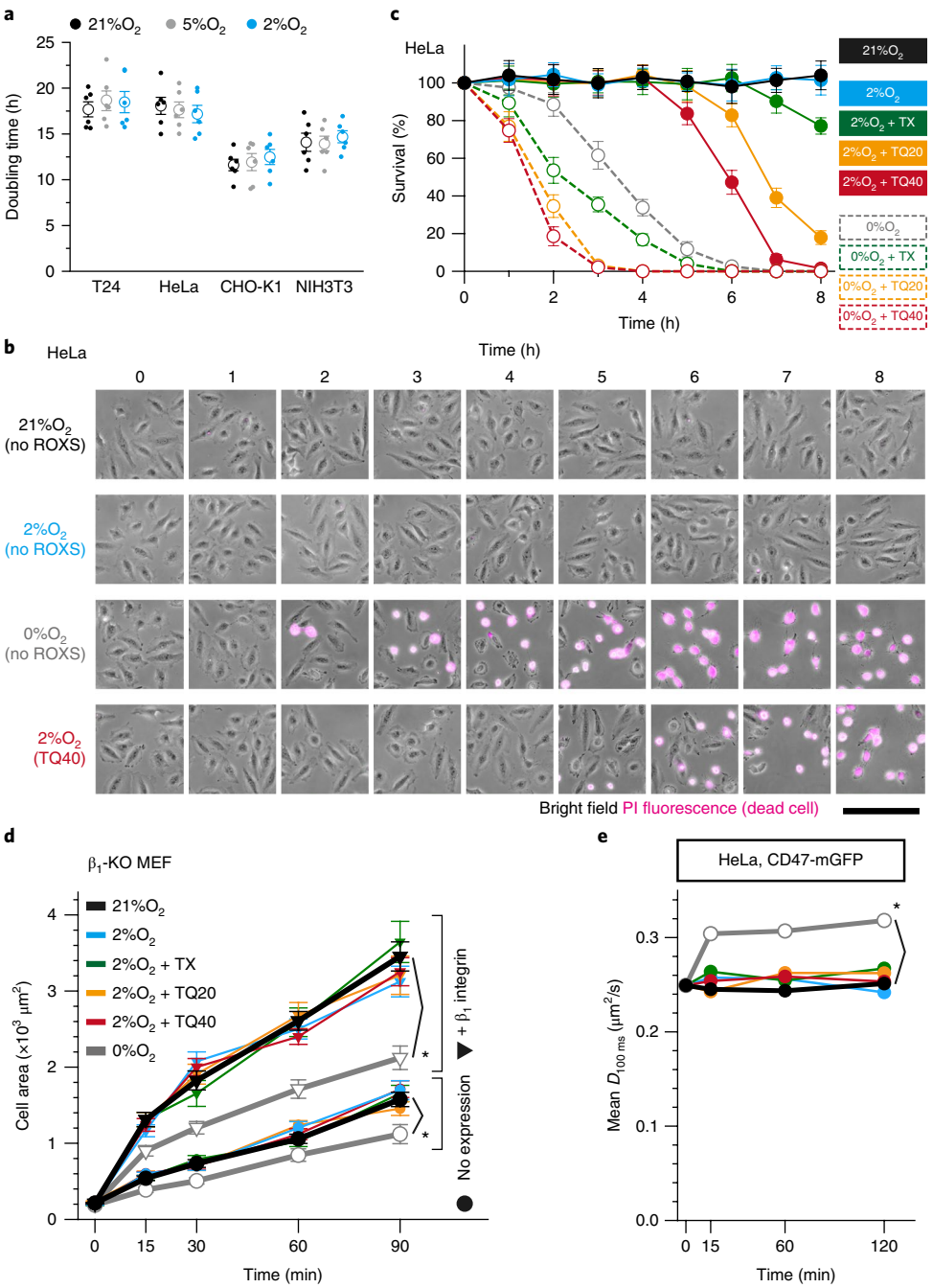

Fig. 3 | No cytotoxicity under 2%O_2, slight toxicity after ROXS addition, in marked contrast to the toxicity of 0%O_2. a, Cellular doubling times at 2%O_2, 5%O_2 or 21%O_2, determined for T24, HeLa, CHO-K1 and NIH3T3 cells. Data are means ± s.e.m. of $n = 6$ independent experiments. No significant differences were found at low oxygen concentrations using a two-sided Welch's t test (P values for 21%O_2 versus 5%O_2 and for 21%O_2 versus 2%O_2, respectively): T24, $P = 0.51$ and $P = 0.59$; HeLa, $P = 0.51$ and $P = 0.59$; CHO-K1, $P = 0.78$ and $P = 0.42$; NIH3T3, $P = 0.91$ and $P = 0.63$. For raw data, see Supplementary Fig. 12. **b**, Representative (among six independent experiments) phase-contrast micrographs of HeLa cells superimposed by their propidium iodide (PI)-stained fluorescence images (pink), recorded for 8 h under various conditions. Scale bar, 200 μm. **c**, Percentages of surviving HeLa cells, under various low-oxygen+ROXS conditions, as determined by the trypan blue exclusion assay ($n = 6$ independent experiments). Data are means ± s.e.m. **d**, Spreading of β_1-KO MEFs (± β_1 integrin expression) after plating on fibronectin (FN)-coated glass-base dishes (Supplementary Fig. 14a). Data are the mean cell areas ± s.e.m. of $n = 20$ cells. 2%O_2+ROXS incubation did not significantly alter the results for up to 90 min. *$P < 0.05$ by two-sided Mann–Whitney U test (for actual P values, see Supplementary Table 5). **e**, Mean diffusion coefficients of CD47-mGFP in HeLa cells, plotted against the incubation times under various conditions (distributions shown in Supplementary Fig. 16b). See Supplementary Fig. 16 for n values. 2%O_2+ROXS treatment did not significantly alter the diffusion coefficients for up to 120 min. *$P < 0.05$ by two-sided Mann–Whitney U test (actual P values are shown in Supplementary Fig. 16). In d and e, statistically significant changes were found only at 0%O_2 (relative to the control conditions), even for an incubation time of 15 min at 0%O_2.

cyanine dyes were greatly improved as compared to the photostabilities observed when the TSQs were added to the solution, particularly under 0%O_2[1,2,4,6]. Here we performed similar experiments by synthesizing TMR-TX-Halo and AT594-TX-CoA, as well as Cy3-TX-Halo and Cy5-TX-Halo, which were examined previously (Supplementary Fig. 17; single-molecule localization precisions of 21.7–28.7 nm in the *x* and *y* directions).

TMR-TX did not show any improved photostability under all of the O_2 concentrations used here, whereas AT594-TX exhibited ~1.6-fold better photostabilities at 0%O_2 and 2%O_2 than with AT594 at 2%O_2+TQ40 (optimized conditions for AT594) (Supplementary Figs. 18 and 19). The extents of TX-induced photostability were large for Cy5-TX and small for Cy3-TX, in general agreement with the data reported previously[2] (Supplementary Figs. 18 and 19).

Among the dyes conjugated with TSQ, Cy5-TX exhibited the slowest photobleaching, with a lifetime of 44.8 s at 0%O_2 (with a single-molecule localization precision of 26.7 nm; Supplementary Table 1 and Supplementary Video 3). This indicates that ST647, under the optimized conditions of 2%O_2+TQ20 (with a 21.5-nm localization precision), photobleached more slowly than Cy5-TX under the optimized conditions of 0%O_2 (unfavorable conditions for live cells), by a factor of 2.2.

Super-long single-molecule tracking of integrins. ACP–β_1 integrin exhibited the ability to enhance cell spreading as much as the native β_1 integrin (Supplementary Fig. 14), and thus it was considered to be functional. Therefore, ST647-ACP–β_1 integrin was observed at the single-molecule level at video rate, together with the FA marker mGFP-paxillin, at 2%O_2+TQ20 (the optimal conditions for ST647). The mGFP-paxillin domains were classified by area size—either smaller or larger than 0.25 μm^2. The former might include the often called nascent adhesions or focal complexes[22,23] (Supplementary Fig. 20).

Single ACP-tagged β_1 and β_3 integrin molecules entered and exited from FAs and repeatedly exhibited temporary immobilizations, which are referred to as 'temporary arrest of lateral diffusion' (TALL), both inside and outside the FA (Fig. 4a, Supplementary Fig. 21 and Supplementary Videos 4 and 5; also see ref. [24]).

In subsequent experiments, we mostly dealt with the larger FAs because integrin behaviors could be observed much more clearly. Every time integrin molecules exhibited TALL, the TALL duration was measured (here the TALL durations included those for TALL events that ended by either movement or the photobleaching of the molecule). The TALL time fractions against the entire trajectory length inside and outside the FA were, respectively, 78% and 51% for ACP–β_1 integrin, or 83% and 40% for ACP–β_3 integrin (Fig. 4b). Namely, inside the FA, integrin molecules can diffuse but are immobilized about ~80% of the time. Even outside the FA, they underwent TALL half of the time, suggesting that integrins probably have important functions even outside the FA (Fig. 4b).

Theory for obtaining the correct TALL lifetime. After observing many TALL events, we obtained a histogram of TALL durations (Supplementary Figs. 22 and 23). To analyze the distribution of TALL duration, we developed a theory to evaluate the correct TALL lifetime from the experimentally obtained TALL duration distributions, which are skewed by photobleaching of probe molecules and limited observation (recording) durations (T_{rec}). Note that, in single-molecule observations, the time window for observing a molecular event is not uniform; rather, each individual molecule provides a different time window by stochastically following a single-exponential photobleaching lifetime distribution (as shown earlier in this study). Furthermore, the limited length of the observation duration (T_{rec}) affects the experimental raw data of the TALL duration distribution because a TALL event can be truncated by the initial and final ends of the observation period (Supplementary Fig. 37 in Supplementary Note 1). Therefore, we developed a theory for obtaining the correct TALL duration distribution from the raw distribution directly obtained by experiments. This theory will be applicable for obtaining the lifetimes of many single-molecule events.

The detailed theory is provided in Supplementary Note 1. In the present integrin experiments, we selected a T_{rec} of 200 s, so that it would minimally affect the results, knowing that the optimized (minimized) photobleaching rate for ST647 is 1/83.5 (with 2%O_2+TQ20). Under these conditions, the duration distribution of TALL events corrected for photobleaching, in the presence of more than one independent immobile state, $n = 1, 2, \ldots, n_I$, and a single mobile state, $G_{fit}^{nI}(\delta)$, would be given by

$$G_{fit}^{nI}(\delta) = \sum_{n=1}^{n_I} A_n exp[-(k_B + k_{M,n}) \cdot \delta] \quad (1)$$

where A_n represents a complex function of the rate constants for state *n* but can practically be determined, as the fitting parameters $k_{M,n}$ is the rate constant for the transition from the immobile state *n* to the mobile state (defined as $1/\tau_n$, where τ_n is the TALL lifetime for the immobile state *n*) and k_B is the photobleaching lifetime common to all of the states (defined as $1/\tau_B$, where τ_B is the photobleaching lifetime).

Three types of TALLs occur both inside and outside the FA. The histogram for TALL duration of β_1 integrin could be fitted by the sum of three exponential-decay functions (see equation (1)), based on both Akaike's and Bayesian information criteria (Supplementary Tables 2 and 3), with decay time constants (lifetimes) of $\tau_1 = 0.51$ (6% time fraction in the total TALL duration and 68% in terms of the number fraction), $\tau_2 = 4.3$ (12% and 16%, respectively), and $\tau_3 = 43$ s (82% and 16%, respectively) inside the FA, after the correction for photobleaching (Fig. 4b, Supplementary Figs. 22 and 24a, and Supplementary Table 2). β_3 integrin exhibited similar TALL behaviors, except that the lifetime of the longest TALL fraction (τ_3 TALL fraction) was longer (79 s) than that for β_1 integrin (43 s) (Fig. 4b and Supplementary Figs. 22 and 24a).

The majority of TALLs, in terms of the number of events, occurred with the shortest lifetime ($\tau_1 \leq 0.51$ and 0.66 s; 68% and 50% for β_1 and β_3 integrin, respectively; Supplementary Fig. 24a). However, the majority of TALLs, in terms of the time fraction (relative to the sum of all TALL durations), were explained by the relatively small numbers of longest TALL (τ_3) events (Fig. 4b). Notably, there were very few molecules that were immobile much longer than the τ_3 lifetimes of 43 and 79 s for β_1 and β_3 integrin, respectively (Supplementary Table 4; see Supplementary Note 1 for the evaluation method), indicating that these three TALL components could describe virtually all of the TALL events that occurred in the FA region. Notably, the addition of Mn^{2+}, an integrin activator[25], only slightly affected the TALL behaviors of β_1 integrin, but its effect on the TALL behaviors of β_3 integrin was much greater; the τ_3 lifetime was prolonged, and the time fraction of the longest τ_3 component was increased (Fig. 4b and Supplementary Figs. 22 and 24a).

TALLs were induced by the binding of integrins to ECM–actin filaments. The dynamic behaviors of three β_1 integrin mutant proteins, β_1-D130A (no RGD binding),β_1-Y783A/Y795A (mutations in the cytoplasmic domain with no binding to talin, tensin, filamin and kindlin, and thus no linkage to actin filaments) and β_1-D130A/Y783A/Y795A (the combination of the extracellular and intracellular mutations) (the products of *ITGB1*^{D130A}, *ITGB1*$^{Y783A/Y795A}$, and *ITGB1*$^{D130A/Y783A/Y795A}$, respectively) were investigated in HeLa cells (see the cell spreading results in Supplementary Fig. 25)[26,27]. β_1-D130A and β_1-Y783A/Y795A exhibited no longest-lifetime (τ_3) TALL component, but exhibited the middle-lifetime (τ_2) component

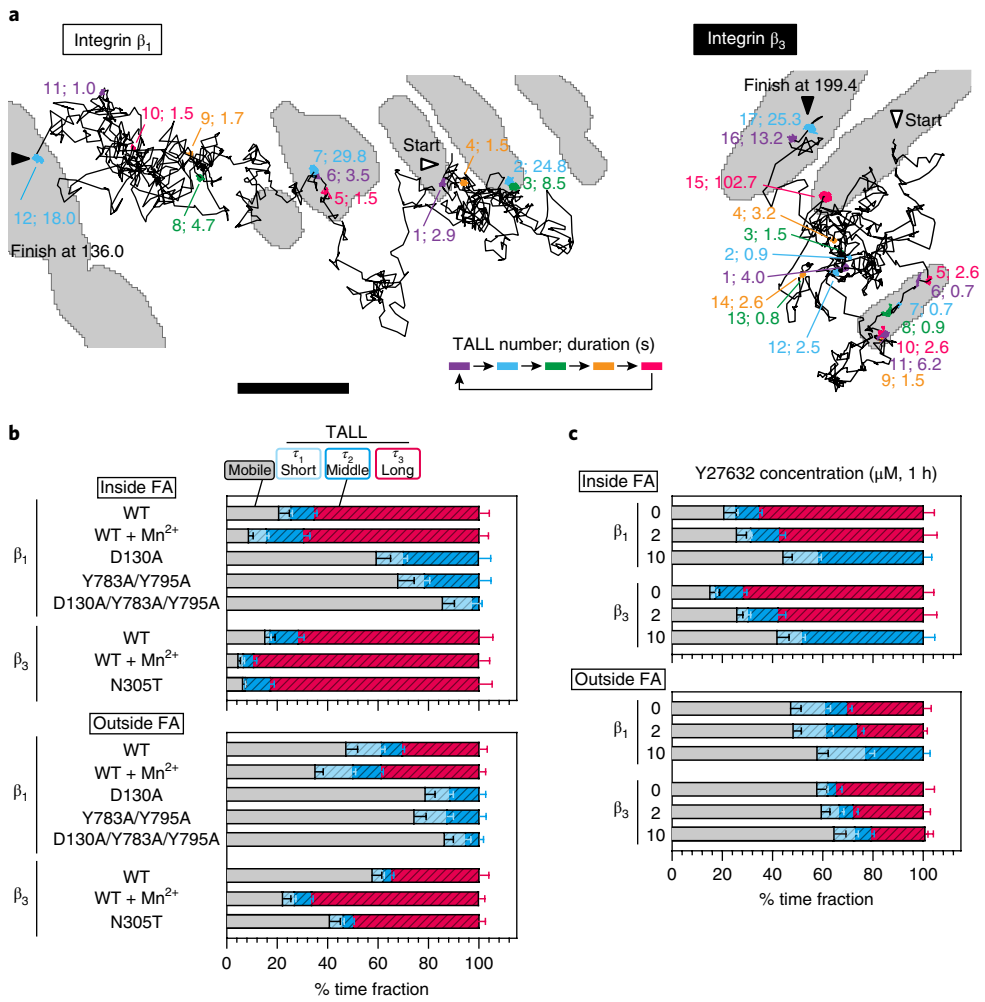

Fig. 4 | Both β_1 and β_3 integrin undergo repeated TALLs, often lasting for 43 and 79 s, respectively, due to binding both the extracellular matrix and actin filaments. a, Typical trajectories of ST647-ACP-β_1 integrin (left) and ACP-β_3 integrin (right) at 2%O_2+TQ20 (among 1,729 and 2,714 trajectories, respectively). The FA zone was visualized by mGFP-paxillin (binarized gray areas). TALLs are shown in color; in each set of numbers shown, the first number indicates the order of occurrences and the second number indicates the TALL duration (s). Scale bar, 2 μm. **b,c**, The time fractions of the periods of the mobile state and the short, middle and long TALL events, inside and outside the FA, for HeLa cells expressing WT (±its activator Mn^{2+}) or mutant β_1 and β_3 integrin proteins (**b**) or before and after treatment with the indicated concentrations of Y27632 (μm) for 1 h (**c**). Data are means ± s.e.m. (for the numbers of observed cells and observed TALL events, see Supplementary Table 2). Fractions that seemed to be immobile were omitted for clarity (Supplementary Tables 2–4 and Supplementary Note 1).

(Fig. 4b and Supplementary Figs. 22 and 24a). β_1-D130A/Y783A/Y795A hardly exhibited even the τ_2 component, and the overall TALL time fraction was decreased to ~15% (Fig. 4b). These results indicate that the middle-length TALL was induced by β_1 integrin binding to either the ECM or the cytoplasmic FA components bound to actin filaments, whereas the longest TALL component was induced by β_1 integrin binding to both the ECM and cytoplasmic FA components.

These results were further confirmed by using a coverslip coated with vitronectin, to which β_1 integrin does not bind[28]. The longest τ_3 component disappeared, supporting the conclusion that this component is due to the binding of β_1 integrin to both the ECM and the actin filament (Supplementary Fig. 26). The time fraction of the τ_3 component of β_3 integrin, which binds to both fibronectin and vitronectin[28], was unchanged, as expected (Supplementary Fig. 26).

Furthermore, the treatment of cells with Y27632, which reduces the traction force on actin filaments by myosin filaments[29] (Supplementary Fig. 26), greatly reduced the τ_3 lifetime and its fraction in a concentration-dependent manner (Fig. 4c and Supplementary Figs. 23 and 24b). Together, these results indicate that integrin molecules linked the ECM and the cytoplasmic actin filaments for the τ_3 periods (exponential distribution) only when the traction force by myosin II was applied to the actin filaments[30–32]. Consistently, the β_3 integrin protein with the hybrid domain swing-out mutation, β_3-N305T (the product of *ITGB3*^{N305T}; refs [33–35]), in which the integrin conformation is locked in the fully extended conformation ready for ECM binding, exhibited a slightly elongated τ_3 and an increased time fraction for the τ_3 component as compared to those of wild-type (WT) β_3 integrin[33–36] (Fig. 4b, Supplementary Figs. 22 and 24a, and Supplementary Table 2).

Even outside the FA, integrin molecules exhibited TALL that was characterized by three lifetime components, although the three TALL lifetimes were reduced as compared to those within the FA (Fig. 4, Supplementary Figs. 21–24 and Supplementary Table 2). Integrins might perform force-related functions both inside and outside the FA[37].

It is not clear how the shortest τ_1 TALL component is induced. Perhaps, before an integrin molecule binds to the ECM and/or

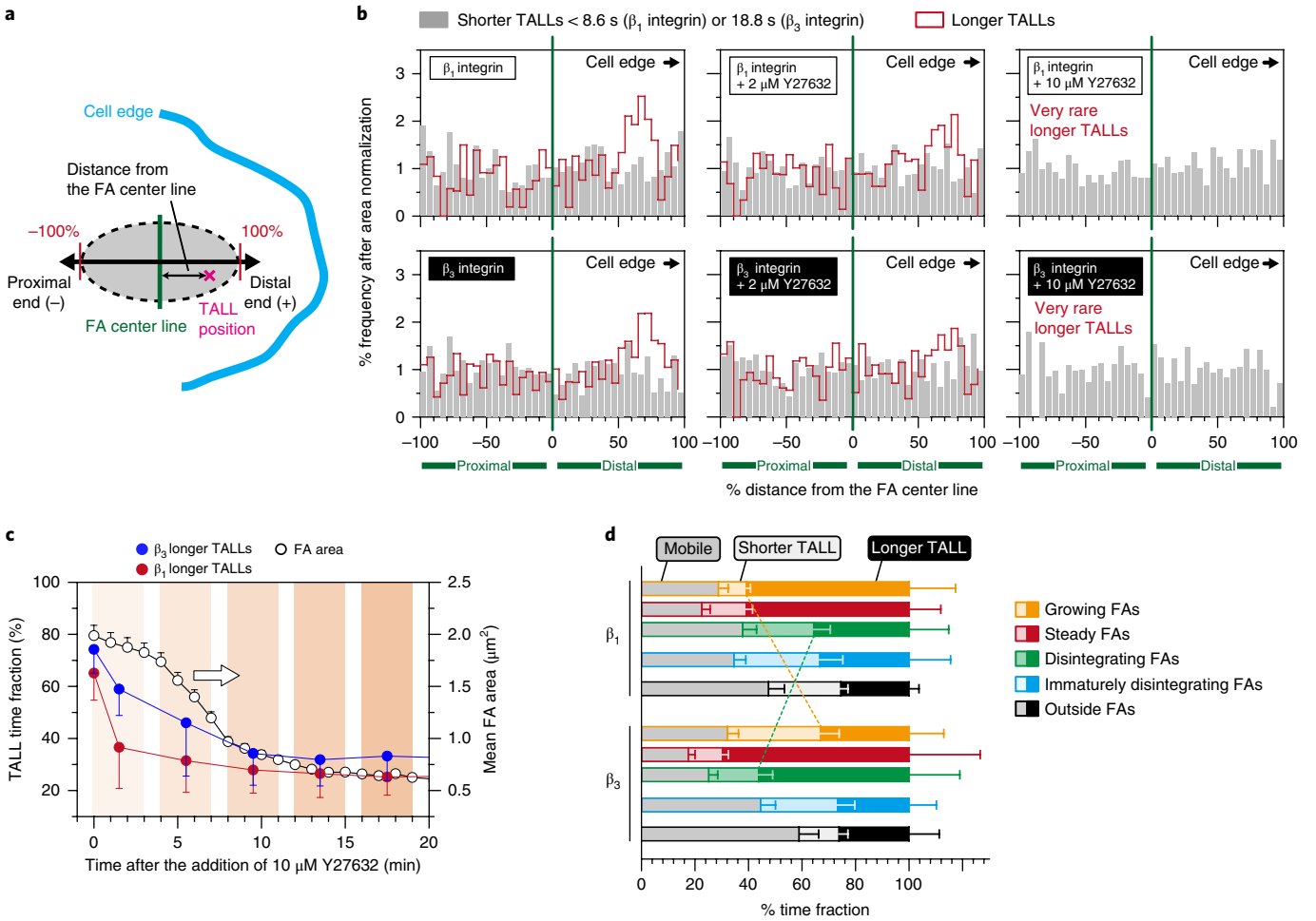

Fig. 5 | Longer TALLs of β_1 and β_3 integrin both occurred most frequently where the traction force was proposed to be largest, whereas in the course of the generation and disintegration of the FAs β_1 integrin arrived at and departed from the FA, respectively, earlier than β_3 integrin. a, Schematic drawing of the FA zone. **b**, Frequencies of longer and shorter TALLs of β_1 integrin (top) and β_3 integrin (bottom) (per unit area, after area normalization), plotted as a function of the location along the FA long axis (distance relative to the half-length of the long axis). For the frequency before the area normalization and the data plotted against the real distance, see Supplementary Fig. 30. For the numbers of inspected TALLs and cells, see Supplementary Table 2. **c**, The time-dependent reductions of the time fractions of longer TALLs of β_1 and β_3 integrin (*y* axis on the left), followed by that of the mean FA area (*y* axis on the right), after treatment with the ROCK inhibitor Y27632.Data are means ± s.e.m. of $n = 32$ cells for mean FA area or of $n = 10$ cells for the TALL time fraction; for clarity, error bars were plotted in only one direction. **d**, The time fractions of longer TALLs, shorter TALLs and mobile periods during the four phases of FA growth and disintegration (relative to the entire trajectory length in time): growing FAs (orange), steady FAs (red), disintegrating FAs (green) and immaturely disintegrating FAs (blue) (for the definition of these phases, see Supplementary Fig. 34). Time fractions outside the FAs are shown in black. Data are means ± s.e.m. of $n = 10$ cells per group.

to actin filaments (through interactions with other proteins), which will induce the τ_2- and τ_3-type TALLs, it might undergo weak interactions with (very transient binding to) the molecules in the ECM and/or actin filaments, which might induce τ_1-type TALLs[31,38].

This concept is consistent with another finding, in which four of five TALLs were the τ_1 and τ_2 types (~80% for both β_1 and β_3 integrin; Supplementary Fig. 24a). This implies that only one of the five shorter TALLs turned into the τ_3 type, which represents 80% of TALLs in terms of the time fraction (Fig. 4b). In summary, we propose that integrin molecules continually reach their sites for binding to the ECM and/or to actin filaments one after another and that once out of approximately five times an integrin molecule becomes bound to both the ECM and the actin filament, thus initiating the longest τ_3-type TALLs.

Integrins' longer TALLs tend to occur at distal FA sites. Because the τ_3-type TALLs were implicated in integrin function, we investigated where they occurred in the FA. For this purpose, TALL events lasting longer than $2 \times \tau_2$ (8.6 s and 18.8 s for β_1 and β_3 integrin, respectively), which represent most of the τ_3 component (86 and 78% for β_1 and β_3 integrin, respectively) and the longer ~15 percentiles of the τ_2 component (for both β_1 and β_3 integrin), were examined, using shorter TALLs that lasted for $< 2 \times \tau_2$ as controls). Longer TALLs of both β_1 and β_3 integrin occurred most often at two-thirds of the distance away from the FA center toward the distal end (also in the presence of Mn^{2+}) in a myosin II–dependent manner, and thus in a traction-force-dependent manner, whereas shorter TALLs occurred uniformly along the FA long axis (Fig. 5a,b and Supplementary Figs. 28–32).

The actual location where the longer TALLs occurred most often was ~0.7 μm away from the FA center toward the distal end,

although the length of the FA long axis varied greatly (2.4 ± 1.3 (mean ± s.d.); Supplementary Fig. 28c). This location is in good agreement with the location where the traction force is highest in the FA[39–41]. Because traction force was required to induce the longer TALLs, we concluded that the longer TALLs are responsible for integrin function by mechanically connecting the ECM and actin filaments in the FA.

Traction force induces integrins' longer TALLs and FA integrity. After cell treatment with 10 μM Y27632, the time fraction of the integrins' longer TALLs decreased rapidly during the initial 1.5 min for β_1 integrin and during the initial 5.5 min for β_3 integrin (Fig. 5c). The mean FA area, as visualized with GFP-paxillin, was decreased by only ~20% during the initial 5 min of the Y27632 treatment, and then further decreased more rapidly between 5 and 15 min (Fig. 5c, Supplementary Fig. 33 and Supplementary Video 6). This result suggests that the integrins' longer TALLs might be important for maintaining FA architecture.

β_1 and β_3 integrin show distinct functions. The occurrence of TALL events in the process of FA maturation and disintegration (in four phases; see Supplementary Fig. 34) was observed (Fig. 5d, Supplementary Fig. 34 and Supplementary Video 7). In the growing phase, β_1 integrin first exhibited large fractions of longer TALLs, whereas β_3 integrin exhibited longer TALLs when the FA was in the mature steady phase (Fig. 5d). In the process of disintegration, the longer TALLs of β_1 integrin were reduced first, whereas β_3 integrin kept displaying longer TALLs for some time (for detailed explanations, see the legend to Supplementary Fig. 34), showing the distinct functions of β_1 and β_3 integrin in the formation, maintenance and disintegration of FAs[36,42,43].

Furthermore, β_1 integrin exhibited a larger fraction of longer TALLs in growing FAs, but ~50% less fractions in immaturely disintegrating FAs (Fig. 5d), whereas β_3 integrin exhibited similar fractions of longer TALLs in both types of FAs. These results indicate that β_1 integrin is responsible for regulating the formation and disintegration of FAs, whereas β_3 integrin is critical for maintaining FAs.

Discussion

Here we found that ST647 (2%O_2+TQ20) is most useful as a membrane-impermeable dye, which allowed for observations of up to 12,000 frames (400 s at video rate). To the best of our knowledge, this is the longest single-fluorescent-molecule tracking ever reported. There are only a few membrane-permeable dyes, but TMR (2%O_2+TX) was found to be the most useful among them, allowing for observations of up to 3,600 frames (120 s at video rate). Under these optimal conditions, the cellular spreading (ECM-binding) functions were unaffected for at least up to 90 min, and the dark state (when the single-dye molecule blinks) lasting for longer than 1 ms was undetectable.

Super-long SMT analyses of β_1 and β_3 integrin revealed that they are frequently, but temporarily, immobilized in various locations within the FA with durations less than 43 s and 79 s, respectively. Taken together with previous results[34,44,45], we concluded that the longer TALLs, which most frequently occurred two-thirds of the distance away from the FA center toward the distal end, were responsible for the mechanical linkage of the actin cytoskeleton to the ECM, in a manner that was dependent on the traction force generated by myosin II (which would induce important conformational changes in the hybrid domain of integrin[34,35,44]; Supplementary Fig. 35).

Methods

Methods, including statements of data availability and any associated accession codes and references, are available at https://doi.org/10.1038/s41589-018-0032-5.

Received: 14 June 2017; Accepted: 5 February 2018;
Published online: 02 April 2018

References

1. Altman, R. B. et al. Cyanine fluorophore derivatives with enhanced photostability. *Nat. Methods* **9**, 68–71 (2011).
2. Altman, R. B. et al. Enhanced photostability of cyanine fluorophores across the visible spectrum. *Nat. Methods* **9**, 428–429 (2012).
3. Lukinavičius, G. et al. A near-infrared fluorophore for live-cell super-resolution microscopy of cellular proteins. *Nat. Chem.* **5**, 132–139 (2013).
4. van der Velde, J. H. M. et al. Mechanism of intramolecular photostabilization in self-healing cyanine fluorophores. *ChemPhysChem* **14**, 4084–4093 (2013).
5. Grimm, J. B. et al. A general method to improve fluorophores for live-cell and single-molecule microscopy. *Nat. Methods* **12**, 244–250 (2015). 3, 250.
6. van der Velde, J. H. M. et al. A simple and versatile design concept for fluorophore derivatives with intramolecular photostabilization. *Nat. Commun.* **7**, 10144 (2016).
7. Giloh, H. & Sedat, J. W. Fluorescence microscopy: reduced photobleaching of rhodamine and fluorescein protein conjugates by *n*-propyl gallate. *Science* **217**, 1252–1255 (1982).
8. Rasnik, I., McKinney, S. A. & Ha, T. Nonblinking and long-lasting single-molecule fluorescence imaging. *Nat. Methods* **3**, 891–893 (2006).
9. Vogelsang, J. et al. A reducing and oxidizing system minimizes photobleaching and blinking of fluorescent dyes. *Angew. Chem. Int. Edn Engl.* **47**, 5465–5469 (2008).
10. Kasper, R. et al. Single-molecule STED microscopy with photostable organic fluorophores. *Small* **6**, 1379–1384 (2010).
11. Cordes, T., Vogelsang, J. & Tinnefeld, P. On the mechanism of trolox as antiblinking and antibleaching reagent. *J. Am. Chem. Soc.* **131**, 5018–5019 (2009).
12. Packer, L. & Fuehr, K. Low oxygen concentration extends the lifespan of cultured human diploid cells. *Nature* **267**, 423–425 (1977).
13. Parsons, M., Messent, A. J., Humphries, J. D., Deakin, N. O. & Humphries, M. J. Quantification of integrin receptor agonism by fluorescence lifetime imaging. *J. Cell Sci.* **121**, 265–271 (2008).
14. Edwald, E., Stone, M. B., Gray, E. M., Wu, J. & Veatch, S. L. Oxygen depletion speeds and simplifies diffusion in HeLa cells. *Biophys. J.* **107**, 1873–1884 (2014).
15. Kusumi, A. et al. Dynamic organizing principles of the plasma membrane that regulate signal transduction: commemorating the fortieth anniversary of Singer and Nicolson's fluid-mosaic model. *Annu. Rev. Cell Dev. Biol.* **28**, 215–250 (2012).
16. Mohyeldin, A., Garzón-Muvdi, T. & Quiñones-Hinojosa, A. Oxygen in stem cell biology: a critical component of the stem cell niche. *Cell Stem Cell* **7**, 150–161 (2010).
17. Semenza, G. L. Oxygen sensing, hypoxia-inducible factors and disease pathophysiology. *Annu. Rev. Pathol.* **9**, 47–71 (2014).
18. Sakadzić, S. et al. Two-photon high-resolution measurement of partial pressure of oxygen in cerebral vasculature and tissue. *Nat. Methods* **7**, 755–759 (2010).
19. Carreau, A., El Hafny-Rahbi, B., Matejuk, A., Grillon, C. & Kieda, C. Why is the partial oxygen pressure of human tissues a crucial parameter? Small molecules and hypoxia. *J. Cell. Mol. Med.* **15**, 1239–1253 (2011).
20. Spencer, J. A. et al. Direct measurement of local oxygen concentration in the bone marrow of live animals. *Nature* **508**, 269–273 (2014).
21. Alejo, J. L., Blanchard, S. C. & Andersen, O. S. Small-molecule photostabilizing agents are modifiers of lipid bilayer properties. *Biophys. J.* **104**, 2410–2418 (2013).
22. Scales, T. M. E. & Parsons, M. Spatial and temporal regulation of integrin signaling during cell migration. *Curr. Opin. Cell Biol.* **23**, 562–568 (2011).
23. Hirata, H., Tatsumi, H., Hayakawa, K. & Sokabe, M. Non-channel mechanosensors working at focal-adhesion–stress-fiber complex. *Pflugers Arch.* **467**, 141–155 (2015).
24. Leduc, C. et al. A highly specific gold nanoprobe for live-cell single-molecule imaging. *Nano Lett.* **13**, 1489–1494 (2013).
25. Mould, A. P. et al. Integrin activation involves a conformational change in the α1 helix of the β-subunit A-domain. *J. Biol. Chem.* **277**, 19800–19805 (2002).
26. Loftus, J. C. et al. A β3-integrin mutation abolishes ligand binding and alters divalent cation-dependent conformation. *Science* **249**, 915–918 (1990).
27. Legate, K. R. & Fässler, R. Mechanisms that regulate adaptor binding to β-integrin cytoplasmic tails. *J. Cell Sci.* **122**, 187–198 (2009).
28. Humphries, J. D., Byron, A. & Humphries, M. J. Integrin ligands at a glance. *J. Cell Sci.* **119**, 3901–3903 (2006).
29. Oakes, P. W., Beckham, Y., Stricker, J. & Gardel, M. L. Tension is required but not sufficient for focal adhesion maturation without a stress fiber template. *J. Cell Biol.* **196**, 363–374 (2012).
30. Kong, F., García, A. J., Mould, A. P., Humphries, M. J. & Zhu, C. Demonstration of catch bonds between an integrin and its ligand. *J. Cell Biol.* **185**, 1275–1284 (2009).

31. Kong, F. et al. Cyclic mechanical reinforcement of integrin–ligand interactions. *Mol. Cell* **49**, 1060–1068 (2013).
32. Livne, A. & Geiger, B. The inner workings of stress fibers—from contractile machinery to focal adhesions and back. *J. Cell Sci.* **129**, 1293–1304 (2016).
33. Cluzel, C. et al. The mechanisms and dynamics of αvβ3 integrin clustering in living cells. *J. Cell Biol.* **171**, 383–392 (2005).
34. Wehrle-Haller, B. Assembly and disassembly of cell matrix adhesions. *Curr. Opin. Cell Biol.* **24**, 569–581 (2012).
35. Li, J. & Springer, T. A. Integrin extension enables ultrasensitive regulation by cytoskeletal force. *Proc. Natl Acad. Sci. USA* **114**, 4685–4690 (2017).
36. Rossier, O. et al. Integrins β1 and β3 exhibit distinct dynamic nanoscale organizations inside focal adhesions. *Nat. Cell Biol.* **14**, 1057–1067 (2012).
37. Wang, Y. & Wang, X. Integrins outside focal adhesions transmit tensions during stable cell adhesion. *Sci. Rep.* **6**, 36959 (2016).
38. Jiang, G., Giannone, G., Critchley, D. R., Fukumoto, E. & Sheetz, M. P. Two-piconewton slip bond between fibronectin and the cytoskeleton depends on talin. *Nature* **424**, 334–337 (2003).
39. Plotnikov, S. V., Pasapera, A. M., Sabass, B. & Waterman, C. M. Force fluctuations within focal adhesions mediate ECM-rigidity sensing to guide directed cell migration. *Cell* **151**, 1513–1527 (2012).
40. Blakely, B. L. et al. A DNA-based molecular probe for optically reporting cellular traction forces. *Nat. Methods* **11**, 1229–1232 (2014).
41. Morimatsu, M., Mekhdjian, A. H., Chang, A. C., Tan, S. J. & Dunn, A. R. Visualizing the interior architecture of focal adhesions with high-resolution traction maps. *Nano Lett.* **15**, 2220–2228 (2015).
42. Roca-Cusachs, P., Gauthier, N. C., Del Rio, A. & Sheetz, M. P. Clustering of $\alpha_5\beta_1$ integrins determines adhesion strength, whereas $\alpha_v\beta_3$ and talin enable mechanotransduction. *Proc. Natl Acad. Sci. USA* **106**, 16245–16250 (2009).
43. Schiller, H. B. et al. β_1- and α_v-class integrins cooperate to regulate myosin II during rigidity sensing of fibronectin-based microenvironments. *Nat. Cell Biol.* **15**, 625–636 (2013).
44. Wehrle-Haller, B. Structure and function of focal adhesions. *Curr. Opin. Cell Biol.* **24**, 116–124 (2012).
45. Doyle, A. D. & Yamada, K. M. Mechanosensing via cell-matrix adhesions in 3D microenvironments. *Exp. Cell Res.* **343**, 60–66 (2016).

Acknowledgements

We thank M. Sokabe (Nagoya University) for the T24 cell lines, M. Kinoshita (Nagoya University) for the NIH3T3 cell lines, M. Humphries (University of Manchester) for the *Itgb1*-knockout MEFs, E. Brown (Genentech) for the human *CD47* cDNA, J. C. Jones (Northwestern University) for the *ITGB3* cDNA, Y. Miwa (Tsukuba University) for the pOStet15T3 vector, T. Goto for the help in some experiments and all members of the Kusumi laboratory for valuable discussions. This work was supported in part by Grants-in-Aid for Scientific Research from the Japan Society for the Promotion of Science (DC1 to T.A.T. (2162), Kiban B to K.G.N.S. (15H04351), Kiban B to T.K.F. (16H04775), and Kiban A and Kiban S to A.K. (24247029 and 16H06386, respectively)), Grants-in-Aid for Innovative Areas from the Ministry of Education, Culture, Sports, Science and Technology of Japan to T.K.F. (15H01212), and a grant from the Core Research for Evolutional Science and Technology (CREST) project of 'Creation of Fundamental Technologies for Understanding and Control of Biosystem Dynamics' of the Japan Science and Technology Agency (JST) to A.K. (JPMJCR14W2). WPI-iCeMS of Kyoto University is supported by the World Premiere Research Center Initiative (WPI) of the MEXT.

Author contributions

T.A.T. performed a large majority of the single-fluorescent-molecule tracking experiments and prepared trolox; Y.W., J.G. and K.N. performed some of the single-fluorescent-molecule tracking experiments to examine the effects of O_2 and ROXS on the photobleaching of fluorescent dye molecules, under the guidance of T.A.T.; T.K.F. and A.K. developed the single-molecule imaging camera system, set up the single-molecule instruments and developed the analysis software; R.S.K., K.G.N.S., T.K.F. and A.K. participated in extensive discussions during the course of this research; T.A.T., T.K.F. and A.K. conceived and formulated this project, and evaluated and discussed data; T.A.T. and A.K. wrote the manuscript; and all of the authors participated in revising the manuscript.

Competing interests

The authors declare no competing interests.

Additional information

Supplementary information is available for this paper at https://doi.org/10.1038/s41589-018-0032-5.

Reprints and permissions information is available at www.nature.com/reprints.

Correspondence and requests for materials should be addressed to A.K.

Publisher's note: Springer Nature remains neutral with regard to jurisdictional claims in published maps and institutional affiliations.

Methods

Cell culture and transfection. T24 cells, a kind gift from Masahiro Sokabe (Nagoya University)[46], HeLa cells (purchased from RIKEN cell bank, RCB0007) and CHO-K1 cells (purchased from Dainippon Pharma Co., Ltd., Osaka, 03-402) were cultured in Ham's nutrient mixture F12 (Sigma-Aldrich), supplemented with 10% (vol/vol) fetal bovine serum (FBS, Life Technologies). NIH3T3 cells (a kind gift from Makoto Kinoshita (Nagoya University))[47] were cultured in Dulbecco's modified Eagle's medium (DMEM, Sigma-Aldrich), supplemented with 10% (vol/vol) FBS. The β1-KO (*Itgb1*-knockout) MEFs were a kind gift from Martin Humphries (University of Manchester)[13]. The cells were cultured in DMEM supplemented with 10% (vol/vol) FBS and 20 U/ml interferon (IFN)-γ (Sigma-Aldrich), at 33 °C. About 24 h before use, the culture medium was replaced by DMEM supplemented with 10% (vol/vol) FBS without IFN-γ at 37 °C. All cell lines were tested for mycoplasma contamination with MycoAlert (Lonza). The identities of the T24 and HeLa cell lines were authenticated by PowerPlex16 STR (contracted to Promega).

For fluorescence microscopy of the cells, the cells were always plated in 12-mm-glass-bottom dishes (Iwaki, Tokyo), pre-coated with fibronectin (FN, Sigma-Aldrich) by placing 10 μg/ml FN on the glass for 1 h at room temperature. The cells were cultured in the growth medium for 24–48 h. Before observation, the culture medium was replaced by the observation medium, T-HBSS. For the experiments involving observing the effect of integrin activation with Mn^{2+}, the cells were cultured in the presence of 1 mM $MnCl_2$ for 1 h before microscope observations.

T24 cells were transfected with the cDNAs encoding CD47 linked to various tag proteins using Lipofectamine LTX (Life Technologies), according to the manufacturer's recommendations. HeLa cells, MEFs and β_1-KO MEFs were transfected with the cDNAs encoding WT β_1 and β_3 integrin and their various mutants, using an electroporator (Nucleofector 2, Lonza; CLB solution and program I-13 for HeLa cells; CLB solution and program A-23 for MEFs), according to the manufacturer's recommendations.

cDNA construction. The cDNA encoding human *CD47* isoform 2 was a kind gift from Eric Brown (Genentech) (NCBI reference sequence: NM_198793.2)[48]. The cDNA encoding human *ITGB1* isoform β-1A was purchased from the NITE Biological Resource Center (NBRC, Tokyo, accession number: AK291697, http://getentry.ddbj.nig.ac.jp/getentry?accession_number=AK291697; NCBI reference sequence: NM_002211.3). The cDNA encoding human *ITGB3* was a kind gift from Jonathan C. Jones (Northwestern University) (NCBI reference sequence: NM_000212.2)[49]. The human paxillin isoform alpha cDNA was cloned from the WI38 cell line (NCBI reference sequence: NM_002859.3). The cDNAs encoding acyl carrier protein (ACP), Halo7 and mGFP (A206K) were obtained from New England Biolabs, Promega and Clontech, respectively. A linker sequence of five amino acids (Ser-Gly-Gly-Gly-Gly) was inserted between the target protein and ACP or mGFP, whereas a 15 amino acid linker ($(Ser\text{-}Gly\text{-}Gly\text{-}Gly\text{-}Gly)_3$) was inserted between the target protein and Halo7. When a tag protein was attached to the N terminus of a transmembrane protein, an additional signal sequence was attached to the N terminus of the tag protein; i.e., the signal peptide (SP) of CD47 for ACP-CD47, the SP of IL-6 for Halo7-CD47, and the SP of CD8 for ACP–β_1 integrin and ACP–β_3 integrin. For the generation of the β_1 integrin mutants $ITGB1^{D130A}$, $ITGB1^{Y783A/Y795A}$ and $ITGB1^{D130A/Y783A/Y795A}$, site-directed mutagenesis was performed using an Agilent Technologies QuikChange site-directed mutagenesis kit. The sequences encoding ACP-CD47, Halo7-CD47, CD47-Halo7 and CD47-mGFP were subcloned into the pOStet15T3 vector (an episomal vector based on the Epstein–Barr virus that carries the tetracycline-regulated expression units: the transactivator (rtTA2-M2) and the *tetO* sequence (a Tet-on vector)). The sequences encoding mGFP-paxillin, β_1 integrin, ACP–β_1 integrin (WT and mutant), β_1 integrin–mGFP and ACP–β_3 integrin (WT and mutant) were subcloned into the pEGFP vector (Clontech). For the details of the cDNA constructs including the linker sequences, see Supplementary Fig. 36.

Fluorescent dyes and fluorescent labeling. Atto488 (AT488)-CoA, DY547-CoA and DY647-CoA were purchased from New England Biolabs. Tetramethylrhodamine (TMR)-Halo, Alexa488 (AL488)-Halo and R110-Halo ligands were purchased from Promega. The syntheses of CoA ligands conjugated with fluorescent dye molecules, TMR, AT594, AT647N and ST647 (TMR-CoA, AT594-CoA, AT647N-CoA and ST647-CoA, respectively), and those of Halo ligands conjugated with AT594 and ST647 (AT594-Halo and ST647-Halo ligands, respectively), as well as those of the CoA and Halo ligands that were linked to fluorescent compounds, Cy3, Cy5, TMR and AT594, by way of TX (Cy3-TX-Halo, Cy5-TX-Halo and TMR-TX-Halo ligands, and AT594-TX-CoA, respectively) are described in Supplementary Note 2. The chemical syntheses of fluorescently conjugated Halo ligands and CoA compounds were performed by Shinsei Chemical Co., Ltd. (Osaka, Japan).

ACP-tagged CD47 and WT and mutant integrins expressed on the cell surface (ACP tag in the extracellular N terminus) were covalently labeled with fluorescent dye compounds by incubating the cells with 50 nM dye-conjugated CoA and 2 μM ACP synthase (New England Biolabs) in the complete growth medium (containing 10 mM $MgCl_2$, which was sufficient for activating the synthase) at 37 °C for 15 min. Halo7-tagged proteins expressed in the PM (both inside and outside the cell) were covalently conjugated with fluorescent organic molecules by incubating the cells with 5 nM Halo ligands linked to TMR or AL488 in the complete growth medium at 37 °C for 15 min, or with 5 nM R110-Halo-ligand in the complete growth medium at 37 °C overnight. Under these conditions, 10~20% of expressed proteins were fluorescently labeled.

Microscopy observations of the cells at various O_2 concentrations. To maintain the cells at 37 °C during the microscopy observation period, the entire microscope, except for the excitation arm and the detection arms, was placed in a microscope environment chamber made with thermo- and electric-field-insulating plastic, and three heating circulators (SKH0-112-OT, Kokensya, Tokyo, Japan) were placed in the box to supply warmed air and to slow air circulation within the box (Supplementary Fig. 3a). A stage-top incubator (Tokai hit, Tokyo, Japan) was placed on the microscope stage for further stabilization of the temperature and for varying the partial pressure of molecular oxygen in the gas environment (Supplementary Fig. 3a). The bottom plane of the chamber had a hole in which a glass-base dish could be placed snugly, to let the gas in the chamber escape from the chamber only slowly. On the lid of this chamber, two small holes were made for the tubing to inject the humidified gas mixture and to place the micro-electrode for monitoring dissolved oxygen concentrations.

The N_2 gas and air ($79\%N_2+21\%O_2$) were supplied from each tank and mixed with a multi-gas mixer (Log MIX, FRONT Co., Ltd., Tokyo, Japan) with flow meters. The gas mixture was humidified by passage through a bottle filled with ultrapure water and was then continuously supplied to the surface of the solution covering the cells attached to the glass-base dish at a flow-rate of 200 ml/min. The dissolved O_2 concentration in the cell-culture medium was directly monitored with a microdissolved-oxygen electrode (DO-166MT; Lazer Research Laboratories, Los Angeles, CA, USA) or a fluorescence-based micro-oxygen probe (MicroTX3; PreSens Precision Sensing GmbH, Regensburg, Germany). The dissolved O_2 concentration in the medium was adjusted by varying the air fraction of the equilibrating gas mixture. When the concentration of the O_2 in the gas mixture was changed, the dissolved O_2 concentration in the specimen was stabilized at the new concentration within 4 min (Supplementary Fig. 3b). In this gas-environment chamber, probably due to the leakage of atmospheric oxygen, oxygen concentrations <0.5% were difficult to attain.

To further reduce the dissolved oxygen concentrations below the sensor's detection limit of $0.05\%O_2$, an enzymatic method was used. The culture medium was replaced with TES–HBSS buffer containing 0.5 mg/ml glucose oxidase and 40 μg/ml catalase, with or without ROXS, supplemented with 2% glucose (instead of the normal 0.1% glucose; for a sufficient supply of glucose) and 20 mM TES (instead of 2 mM TES; for pH stabilization against pH decreases due to the generation of gluconic acid by the enzymatic reactions to reduce the dissolved oxygen concentration) (GLOX buffer). When the surface of the GLOX buffer in the glass-base dish was left uncovered, owing to the newly dissolved O_2 from the atmosphere in the GLOX buffer, the glucose oxidase–catalase system continually generated gluconic acid (thus lowering the pH), which might have affected the live cells. To suppress the further influx of molecular oxygen into the GLOX buffer, a round cover made of aluminum foil was placed on the surface of the GLOX buffer. This effectively blocked the pH changes of the GLOX buffer, and the dissolved O_2 concentration was maintained below the detection limit for at least 2 h (<0.05%; Supplementary Fig. 3b). For longer-term incubation periods, the GLOX buffer was replaced every 2 h to prevent acidification.

ROXS solution preparation. Trolox was first dissolved in dry DMSO at a concentration of 0.5 M, and then diluted in T-HBSS. Troloxquinone was generated by UV (UVP, 302 nm, 15 W)-induced oxidation of 1.5 mM trolox in ultrapure water with air bubbling (to supply O_2) until the troloxquinone/trolox ratio reached 0.6:0.4 (typically in 10–20 min), as described previously[11] (Supplementary Fig. 4). The troloxquinone/trolox ratio in the solution was determined by measuring the optical density at 255 nm, as described previously[11], using an optical absorption spectrometer (U-3900H, Hitachi). A stock solution containing trolox and troloxquinone, at a molar ratio of 4:6, was produced by mixing this solution (prepared by UV-induced oxidation) with the TX solution; this was stored at 4 °C in the dark and used within a week. In the present research, the final concentration of trolox+troloxquinone was always 1 mM (in T-HBSS).

Assays for cell growth, cytotoxicity and cell spreading. To examine cell growth, cells were seeded in complete growth medium in 6-well tissue culture dishes (35-mm diameter; Iwaki) and cultured under a gas mixture containing 5% CO_2 and $21\%O_2$, $5\%O_2$ or $2\%O_2$ (+74%, 90%, or 93% N_2, respectively), using a multi-gas incubator MG-70M (Taitec, Tokyo), at 37 °C. Cells were removed from the culture dish every ~12 h, using the standard trypsin solution used in our study (0.25% trypsin and 1 mM EDTA in 10 mM PBS, pH 7.4), and mixed with a trypan blue solution; the live cells, which were not stained with trypan blue, were counted with a hemocytometer. The experiments were repeated for six independent specimens, and the mean ± s.e.m. was determined.

To quantitatively examine cell survival in the presence of ROXS reagents at $21\%O_2$ and $2\%O_2$ atmospheres in a time course up to 8 h, cells were plated on

FN-coated 35-mm tissue culture dishes and cultured in the complete growth medium for ~24 h. The medium was then replaced by T-HBSS that was prewarmed to 37 °C, with or without ROXS reagents. For experiments involving <0.05% dissolved oxygen (which is the detection limit of the sensor employed here), the GLOX buffer was used. Cells were removed from the culture dish by the standard trypsin solution every ~1 h. The number of live cells was evaluated as described for the cell growth assay.

For examining cell survival by imaging, cells cultured on FN-coated glass-base dishes were stained with 10 ng/ml PI in T-HBSS for 5 min and then fixed with 4% paraformaldehyde for 15 min. After fixation, phase-contrast and fluorescence microscopic images of the cells were obtained with an Olympus IX70 inverted epifluorescence microscope equipped with a 60×1.25 numerical aperture (NA) Plan Apo objective lens and an Andor-Clara cooled charge-coupled device (CCD) camera.

The influences of low oxygen concentrations and/or the presence of ROXS reagents on the spreading of β_1-KO MEFs and β_1-KO MEFs that were transfected with constructs encoding WT or modified β_1 integrin molecules on FN-coated glass-bottom dishes were examined. β_1-KO MEFs were transfected with the cDNAs encoding various β_1 integrin proteins by electroporation, as described in the subsection "Cell culture and transfection," cultured for 18 h, removed from the cell culture dish by trypsinization for 3 min, allowed to recover in the complete growth medium for 1 h, and then replated on FN-coated glass-bottom dishes in T-HBSS with or without ROXS or in the GLOX buffer with or without ROXS. At selected time points after plating, the cells were fixed with 4% paraformaldehyde for 1 h, incubated with 100 mM glycine for 15 min, permeabilized with 0.1% Triton X-100 for 5 min and then further incubated with 1% BSA for 1 h. The cells were then immunostained with 20 μM anti–β_1 integrin monoclonal antibody (K-20, also called 'neutral mAb', which recognizes both active and inactive β_1 integrin; Santa Cruz) for 1 h and then with 5 μM rhodamine red-X-labeled anti-mouse-IgG secondary antibody (Jackson ImmunoResearch, 715-295-151) for 1 h. Microscopic observations were conducted as described in the previous paragraph. The cell area (parameter for evaluating cell spreading) was measured in the phase-contrast images, using ImageJ software. Results are described as means ± s.e.m. for 20 cells.

Confocal imaging of mGFP-paxillin and Alexa647-conjugated phalloidin in cells before and after the treatment with the ROCK inhibitor Y27632. HeLa cells expressing mGFP-paxillin, which were plated on FN-coated glass-base dishes, were incubated with 1–10 μM Y27632 in T-HBSS for 1 h. The cells were then fixed with 4% paraformaldehyde for 1 h and incubated with 100 mM glycine for 15 min, 0.1% Triton X-100 for 5 min, 1% BSA for 1 h and then 500 nM Alexa647-phalloidin (Life Technologies) for 30 min, followed by embedding in Permafluor (Thermo Scientific) for confocal fluorescence microscopy (Olympus, FV1000) (Supplementary Fig. 27a).

Single-fluorescent-molecule imaging. Fluorescently labeled molecules located in the basal PM (the ventral PM; i.e., the PM facing the coverslip), and those attached to the coverslip, were illuminated with an evanescent field and observed at 37 °C, using home-built objective-lens-type TIRF microscopes, which were constructed on Olympus inverted microscopes (IX-81 and 70 for video-rate and high-speed observations, respectively) equipped with Olympus 100×1.49 NA objective lenses. The fluorescence images were projected onto a two-stage microchannel plate intensifier (C8600-03; Hamamatsu Photonics), which was lens-coupled to an electron bombardment CCD camera (C7190-23; Hamamatsu Photonics) operated at video rate or was optical-fiber-bundle-coupled to a high-speed complementary metal oxide semiconductor sensor camera (Focuscope SV-10k; Photron) operated at 1 and 10 kHz (256×256 pixels)[50].

The incident excitation laser power at the exit of the objective lens was 1.98 mW for the 488-nm line (for AT488, AL488, and R110), 2.31 mW or 4.60 mW for the 561-nm line (for TMR or DY547 and Cy3-TX, respectively), 1.17 mW for the 594-nm line (for AT594), and 1.06 mW or 3.18 mW for the 642-nm line (for DY647, AT674N, and ST647 or Cy5-TX, respectively). For high-speed observations of TMR (561-nm line), 10.8 and 108 mW were used for the observation frame rates of 1 and 10 kHz, respectively.

Each individual fluorescent spot in the image was identified and tracked by using a home-made computer program, as described previously[51]. The superimposition of images in different colors obtained by two separate cameras was conducted as described previously[50].

Methods to measure photobleaching lifetimes and durations in which single molecules could be tracked, and the mean signal intensity of single fluorescent spots. As a convenient measure for the photobleaching lifetime, the 'number-counting lifetime' measure was used. In this method, after obtaining image sequences at video rate, the number of fluorescence spots detected in each video frame was obtained and plotted against time, and then the numbers of spots in each frame (time bin) obtained in all of the image sequences were added together. We found that these plots of the (total) number of fluorescent spots versus time for all of the dye molecules under all of the ROXS conditions used here could be fitted by single-exponential functions. Therefore, the exponential decay constants (mean ± s.e.m.) were defined as the number-counting lifetime. The number-counting photobleaching lifetime would virtually be the same as the lifetime evaluated by the bulk intensity measurements.

As another method, the 'single-molecule tracking lifetime' was used. In this method, we measured the duration in which each fluorescent spot was detectable, starting from the initiation of the observation by turning on the excitation laser (time 0; until the first transition to the dark state; this way, we only observed the molecules that were visible at time 0). After observing many single molecules, we obtained the histogram for the bright-state durations. This histogram might resemble that for the on-time distributions, but because it was observed from the start of excitation laser illumination, rather than the onset of fluorescence emission during steady-state illumination, the actual values would be different. However, we used this method because it would provide the lifetime more relevant to actual experiments conducted using live cells, as it provides the distribution of the lengths of single-molecule trajectories observed from time 0 (starting of laser excitation). We found that the distributions for all of the molecules under all of the ROXS conditions used here could operationally be fitted by single-exponential functions; the exponential decay constants (means ± s.e.m.) were used as 'single-molecule tracking lifetimes'.

The mean (± s.e.m.) fluorescence intensity of single fluorescence spots was obtained in the following way. After measuring the fluorescence signal intensities of all the fluorescence spots, the distribution of the intensities was fitted by a log-normal function, and the mean intensity was obtained as the value of the mode of the log-normal function.

Note that in these determinations, the s.e.m. is provided as the fitting error of the 68.3% confidence limit. In such determinations, the number of independent experiments is given as the degree of freedom for fitting (ν), which equals 'the number of bins used for the fitting' minus 'the number of free parameters used for the fitting'. However, because the number of total fluorescence spots and the number of events (various events observed in the present research, such as the TALL events) would also be useful for clarifying the conducted experiments, in addition to the degree of freedom, we describe the numbers of independent experiments and the numbers of observed molecules, events or cells, wherever appropriate.

Long-term tracking of single integrin molecules inside and outside the FA. HeLa cells transfected with sequences encoding ACP-integrins (WT and mutant β_1 integrin and β_3 integrin) and mGFP-paxillin were cultured for 24–48 h on FN-coated glass-bottom dishes, and the ACP-integrins were labeled with ST647-CoA by the same method used for labeling ACP-CD47. For the long-term tracking of single individual integrin molecules inside and outside FAs, the stage drift was corrected by using 100-nm fluorescent tetraspeck beads (Life Technologies) that were attached to the glass surface in the specimen as fiducial markers.

Single ST647 molecules attached to the coverglass of the glass-base dish were observed at a video rate for 6,000 frames (200 s), and after correcting for the long-term drift using the fiducial markers, the localization precisions of single ST647 molecules (31 molecules) were found to be 26 nm for both the x and y coordinates. These values should be compared with the localization precision for short-term observations (100 frames ~3 s) of 22 nm. This result showed that long-term tracking, such as 6,000 frames, could be performed at localization precisions comparable to those attainable for much shorter trajectories, such as 100 frames, after correction for the stage drift.

Transient-immobilization or TALL events were detected in single-molecule tracking trajectories, by using the algorithm developed by Sahl et al.[52] and modified by Shibata et al.[53]. The detection circle (magnifying-glass) radius and the threshold residency time were set at 200 nm and 20 frames (0.67 s), respectively. Using these parameter values, the TALL time fractions in Monte-Carlo-generated simple-Brownian trajectories with diffusion coefficients of 0.16 and 0.27 $\mu m^2/s$, which are the mean diffusion coefficients for β_1 integrin inside and outside the FA region, respectively, were found to be only 1.42 ± 0.02% and 0.26 ± 0.01%, respectively.

To identify and define the FA areas, mGFP-paxillin was expressed in cells and used as an FA marker. The cells that expressed both mGFP-paxillin and ACP-integrin were selected. First, the mGFP-paxillin images were recorded for 3.3 s (100 video frames, not at the level of single molecules); subsequently, the ST647-labeled ACP-integrin was observed for 6,000 frames (200 s) at the level of single molecules. Consistent with the results described by Shibata et al.[53], the changes in the FA morphology during ~200 s were limited, and therefore, the mGFP-paxillin image sequence obtained before the single-molecule observations of integrins was used to define the FA areas. The entire image sequence of 100 frames was averaged, and the resulting image was binarized to determine the boundaries between the FA regions and the bulk PM domain. The threshold pixel value used for binarization was found by using an adaptive thresholding algorithm. For the successful binarization of both the larger and smaller FAs, the images before and after Laplacian filtering were binarized, and then the binarized images were compared. For further details, see Supplementary Fig. 20 and its legend. All integrin trajectories were subdivided into those inside and outside the FA zones, and then analyzed.

Software and statistical analysis. TIRF images of FAs were processed and analyzed using ImageJ for Windows or MatLab 2012a for Windows. Superimposition

of image sequences obtained in two colors and single-molecule tracking were performed using C++-based computer programs produced in-house, as described previously[50,51]. Statistical analysis was performed by two-sided Welch's *t*-test or two-sided Mann–Whitney *U* test using OriginPro 2015 for Windows. $P < 0.05$ was considered to be statistically significant. Curve fitting and its examination using Akaike's and Bayesian information criteria were performed using OriginPro 2015 for Windows.

Life Sciences Reporting Summary. Further information on experimental design is available in the Life Sciences Reporting Summary.

Data availability. All data generated or analyzed for this study are available within the paper and its associated supplementary information files. All other data presented and codes written are available upon reasonable request from the corresponding author.

References

46. Naruse, K., Sai, X., Yokoyama, N. & Sokabe, M. Uniaxial cyclic stretch induces c-SRC activation and translocation in human endothelial cells via SA channel activation. *FEBS Lett.* **441**, 111–115 (1998).
47. Ihara, M. et al. Association of the cytoskeletal GTP-binding protein Sept4 (H5) with cytoplasmic inclusions found in Parkinson's disease and other synucleinopathies. *J. Biol. Chem.* **278**, 24095–24102 (2003).
48. Lindberg, F. P., Gresham, H. D., Schwarz, E. & Brown, E. J. Molecular cloning of integrin-associated protein: an immunoglobulin family member with multiple membrane-spanning domains implicated in αvβ3-dependent ligand binding. *J. Cell Biol.* **123**, 485–496 (1993).
49. Tsuruta, D. et al. Microfilament-dependent movement of the β3-integrin subunit within focal contacts of endothelial cells. *FASEB J.* **16**, 866–868 (2002).
50. Koyama-Honda, I. et al. Fluorescence imaging for monitoring the colocalization of two single molecules in living cells. *Biophys. J.* **88**, 2126–2136 (2005).
51. Fujiwara, T., Ritchie, K., Murakoshi, H., Jacobson, K. & Kusumi, A. Phospholipids undergo hop diffusion in compartmentalized cell membrane. *J. Cell Biol.* **157**, 1071–1081 (2002).
52. Sahl, S. J., Leutenegger, M., Hilbert, M., Hell, S. W. & Eggeling, C. Fast molecular tracking maps nanoscale dynamics of plasma membrane lipids. *Proc. Natl Acad. Sci. USA* **107**, 6829–6834 (2010).
53. Shibata, A. C. E. et al. Archipelago architecture of the focal adhesion: membrane molecules freely enter and exit from the focal adhesion zone. *Cytoskeleton* **69**, 380–392 (2012).

nature research

Corresponding author(s): Akihiro Kusumi

☐ Initial submission ☐ Revised version ☒ Final submission

Life Sciences Reporting Summary

Nature Research wishes to improve the reproducibility of the work that we publish. This form is intended for publication with all accepted life science papers and provides structure for consistency and transparency in reporting. Every life science submission will use this form; some list items might not apply to an individual manuscript, but all fields must be completed for clarity.

For further information on the points included in this form, see Reporting Life Sciences Research. For further information on Nature Research policies, including our data availability policy, see Authors & Referees and the Editorial Policy Checklist.

Experimental design

1. Sample size

Describe how sample size was determined.

We performed pilot experiments using smaller sample numbers, and after performing Student t-test, we determined the expected minimal sample size to prove or disprove the hypothesis. We generally did more experiments than this minimal number of experiments.

2. Data exclusions

Describe any data exclusions.

No data exclusions.

3. Replication

Describe whether the experimental findings were reliably reproduced.

All experimental findings were reliably reproduced.

4. Randomization

Describe how samples/organisms/participants were allocated into experimental groups.

All sample allocations were random.

5. Blinding

Describe whether the investigators were blinded to group allocation during data collection and/or analysis.

The sample preparation and observation were mostly preformed by the same operator. Therefore, no blinding was performed.

Note: all studies involving animals and/or human research participants must disclose whether blinding and randomization were used.

6. Statistical parameters

For all figures and tables that use statistical methods, confirm that the following items are present in relevant figure legends (or in the Methods section if additional space is needed).

n/a	Confirmed
☐	☒ The exact sample size (*n*) for each experimental group/condition, given as a discrete number and unit of measurement (animals, litters, cultures, etc.)
☐	☒ A description of how samples were collected, noting whether measurements were taken from distinct samples or whether the same sample was measured repeatedly
☐	☒ A statement indicating how many times each experiment was replicated
☐	☒ The statistical test(s) used and whether they are one- or two-sided (note: only common tests should be described solely by name; more complex techniques should be described in the Methods section)
☐	☒ A description of any assumptions or corrections, such as an adjustment for multiple comparisons
☐	☒ The test results (e.g. *P* values) given as exact values whenever possible and with confidence intervals noted
☐	☒ A clear description of statistics including central tendency (e.g. median, mean) and variation (e.g. standard deviation, interquartile range)
☐	☒ Clearly defined error bars

See the web collection on statistics for biologists for further resources and guidance.

Software

Policy information about availability of computer code

7. Software

Describe the software used to analyze the data in this study.	All the software used is described in the Methods section, under the heading "Software and statistical analysis". Data and code availability statement is now placed as an independent Subsection with the heading "Data and code availability" at the end of the Methods section.

For manuscripts utilizing custom algorithms or software that are central to the paper but not yet described in the published literature, software must be made available to editors and reviewers upon request. We strongly encourage code deposition in a community repository (e.g. GitHub). *Nature Methods* guidance for providing algorithms and software for publication provides further information on this topic.

Materials and reagents

Policy information about availability of materials

8. Materials availability

Indicate whether there are restrictions on availability of unique materials or if these materials are only available for distribution by a for-profit company.	No restricted materials were used in this study.

9. Antibodies

Describe the antibodies used and how they were validated for use in the system under study (i.e. assay and species).	Anti-integrin β1 monoclonal antibody IgG (Santa Cruz, K20) Rhodamine red X-labeled anti-mouse IgG secondary antibody (Jackson Immuno Research 715-295-151) These have been described in the Methods section.

10. Eukaryotic cell lines

a. State the source of each eukaryotic cell line used.	T24 is a kind gift from Masahiro Sokabe of Nagoya University; Naruse, K., Sai, X., Yokoyama, N. & Sokabe, M. FEBS Lett. 441, 111–115 (1998). HeLa is purchased from RIKEN cell bank (RCB0007). CHO-K1 is purchased from Dainippon Pharma Co., Ltd., Osaka (03-402). NIH3T3 is a kind gift from Makoto Kinoshita of Nagoya University; Ihara, M. et al. J. Biol. Chem. 278, 24095–24102 (2003). These are described in the Methods section.
b. Describe the method of cell line authentication used.	The identities of the T24 and HeLa cell lines were authenticated by PowerPlex16 STR (contract to Promega). CHO-K1 and NIH3T3 cell lines were not authenticized. These are described in the Methods section.
c. Report whether the cell lines were tested for mycoplasma contamination.	All cell lines used were proved to be mycoplasma free using MycoAlert (Lonza), and this is described in the Methods section.
d. If any of the cell lines used are listed in the database of commonly misidentified cell lines maintained by ICLAC, provide a scientific rationale for their use.	T24 human epithelial bladder carcinoma cells used in this study were previously misidentified as ECV304 human endothelial cells. We used this cell line here because the structure and molecular dynamics in the plasma membrane have been very well characterized by us as well as many others.

Animals and human research participants

Policy information about studies involving animals; when reporting animal research, follow the ARRIVE guidelines

11. Description of research animals

Provide details on animals and/or animal-derived materials used in the study.	No animals were used in this study.

Policy information about studies involving human research participants

12. Description of human research participants

Describe the covariate-relevant population characteristics of the human research participants.	This study did not involve human research participants.